Carbon 196 (2022) 699–707

Contents lists available at ScienceDirect

Carbon

journal homepage: www.elsevier.com/locate/carbon

Efficient transport system of cultivated mushroom mycelium enables its derived carbon with high performance electrochemical desalination capability

Chen Zhao [a,b,1], Qin Wang [c,1], Shaozhong Chang [a], Shuo Zhang [a], Zhonghua Li [a], Zihan Shen [b], Xin Jin [a], Han Xiao [c,*], Huigang Zhang [a,b,**]

[a] National Laboratory of Solid State Microstructures, Collaborative Innovation Center of Advanced Microstructures, College of Engineering and Applied Sciences, Nanjing University, Nanjing, 210093, China
[b] State Key Laboratory of Multiphase Complex Systems, Institute of Process Engineering, Chinese Academy of Sciences, Beijing, 100190, China
[c] State Key Laboratory of Microbial Metabolism, Joint International Research Laboratory of Metabolic & Developmental Sciences, School of Life Sciences and Biotechnology, Shanghai Jiao Tong University, Shanghai, 200240, China

ARTICLE INFO

Keywords:
Capacitive deionization
Transport
Biomass
Mycelium
Sporophore
Porous carbon

ABSTRACT

Capacitive deionization (CDI) is regarded as a promising desalination technology because of its high efficiency and low energy consumption. Electrode materials with high surface area, abundant active sites, and interconnected pore structure are the key to enhancing the electrochemical performance of CDI devices. Here, we selectively cultivated mushroom mycelia as the precursor to fabricate a hierarchically porous carbon electrode that consists of interwoven and hollow filaments for the CDI. By using the high-efficiency transport system of mycelia that natural evolution endows with, the resultant mycelia-derived carbon (MDC) exhibits a high surface area of 3603 $m^2 g^{-1}$ and delivers a high capacity of 260 F g^{-1}. The assembled CDI devices could realize a superior salt removal capacity of 24.17 mg g^{-1}. Efficient transport system of mycelia enables MDC to rapidly remove salts from solution with an extremely short characterization time. Such a high-efficiency CDI electrode could be attributed to the use of naturally-optimized transport system, high surface area, and heteroatomic surface. In contrast with artificial chemical synthesis, biologic cultivation offers some higher-order structures that conventional technologies would not easily achieve. This work provides an alternative approach to improving the transport of hierarchical CDI electrodes from living things.

1. Introduction

With the growing population and shortage of freshwater, water purification receives an increasing attention [1]. Conventional desalination technologies like evaporation or reverse osmosis, *etc.* Incur excessive energy cost because a large amount of water molecules are separated by phase transformation or pressure [2–4]. Capacitive deionization (CDI) is based on electrochemical adsorption/desorption of ions, which demonstrates advantages for heavy metal and pollutant removal and desalination [5,6]. The CDI devices adsorb cations and anions on their anodes and cathodes (Fig. 1a), respectively, like electrical double-layer capacitors [6–8]. When the voltage polarity is switched, the ions adsorbed by electrodes are released to the extraction solution. Because a minimal work is done to separate salt from solutions, it is expected to consume less energy than other technologies [6]. Either conventional technologies or CDI require materials to have abundant pores for adsorption and mass transport [9,10]. In addition, the CDI performance like other electrochemical devices are highly related to the surface area, pore structure (Fig. 1b), conductivity, wettability, and surface functionality (Fig. 1c) [9,11–13]. To improve these properties for efficient CDI, carbon materials are usually preferred because of their excellent stability, variable forms, and ease for rational design. The

* Corresponding author.
** Corresponding author. National Laboratory of Solid State Microstructures, Collaborative Innovation Center of Advanced Microstructures, College of Engineering and Applied Sciences, Nanjing University, Nanjing, 210093, China.
E-mail addresses: smallhan@sjtu.edu.cn (H. Xiao), hgzhang@ipe.ac.cn (H. Zhang).
[1] C.Z and Q.W. contribute equally to this work.

https://doi.org/10.1016/j.carbon.2022.05.020
Received 19 February 2022; Received in revised form 9 May 2022; Accepted 10 May 2022
Available online 12 May 2022

deterministic properties of CDI carbon materials on ion storage and uptake capability are strongly influenced by the choice of precursors, synthetic conditions, and post-treatment [14,15]. Therefore, the nature of precursors is crucial in fabricating high-order carbon materials.

Biological systems are masters of material synthesis and structure building [16–18]. Evolution endows living organisms with hierarchical structures to efficiently uptake nutrients and transport resources and metabolites [19,20]. High-efficiency transport like some biologic systems is desired for current industrial processes. Biological tissues and/or organs are formed and regulated under the guidance of genes, which contrasts with the artificial synthesis from atomic aggregation or crystallization. Gene-controlled synthesis could lead to a large variety of higher-order structures that artificial technologies hardly realize. In contrast to the wide applications of biosynthesized chemicals, the original functions of the higher-order biological tissues and/or organs are rarely studied or used for industrial applications. High-efficiency transport system is one outstanding feature of biologic structures [21,22]. From microorganisms to plants, or cells to animals, living organisms evolve to develop efficient transport systems of nutrients and metabolites, which are highly organized and work like chemical factories at multiple scales [23]. Transport is of vital importance to chemical industries. Rapid transport could enhance separation and even shift the equilibria of chemical reactions [24,25]. In this work, we focus on electrochemical desalination by using the efficient transport system of biological tissues and/or organs.

Various biomass materials like rice [26], watermelon [27], egg [28], coffee beans [29], citrus [30], *etc.* Have been studied to fabricate porous carbon for the CDI because of their natural hierarchical structures. The resultant CDI devices demonstrate interesting salt adsorption capacity (SAC). However, it has to be noted that some biomass materials in live things, by their originality and nature, may not evolve to work for adsorption/desorption [31]. Conversely, mushroom has been well recognized to specially adsorb metal ions from soil [32–34] because (1) hypha having hollow tube morphology form an interwoven network to transport water or resources [35]; (2) excretion of organic acid could form complex with metal ions [34]; (3) a thin wall may readily uptake metal ions [36]; (4) intravascular flow permits solute transport [37]; (5) surface functional groups (carboxyl (-COOH), amide (-NH_2), thiol (-SH),

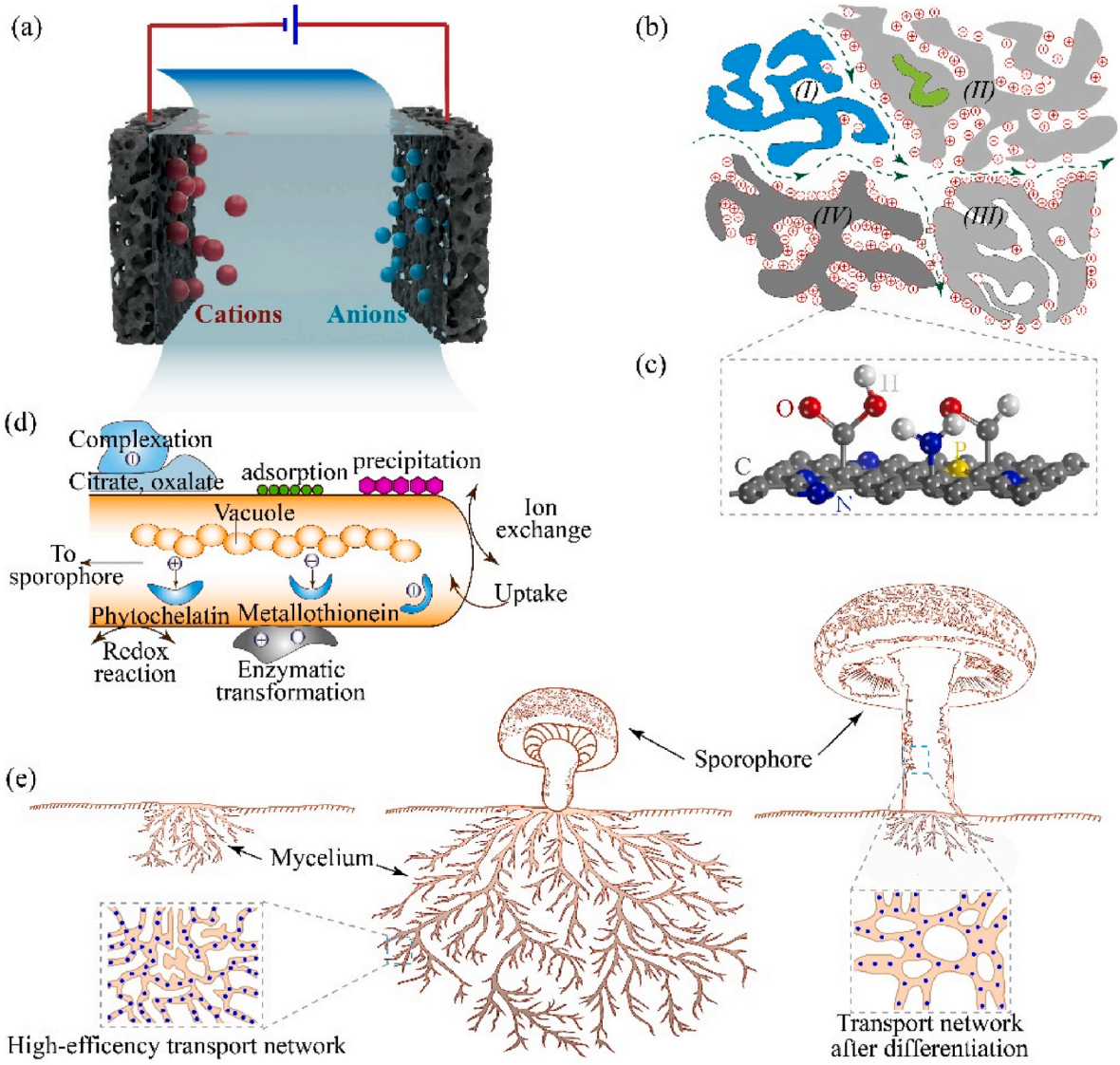

Fig. 1. Schematic diagram of desalination and mycelium-based material design: (a) desalination setup and principles. (b) Active materials with varied structural features: (i) isolated region, (ii) close pores, (iii) tortuous pores, and (iv) interconnected pores. (c) Surface functionality for desalination. (d) Transport system of tubular filaments and the interaction with ions (adapted from Ref. [32]). (e) Typical growth stages from mycelium to sporophore, whose different transport systems offer opportunities to engineer active materials for desalination. (A colour version of this figure can be viewed online.)

phosphate (PO_4^-), and hydroxide (-OH)) may induce adsorption or precipitation of metal ions [38]; (6) ion exchange may include metal ions inside [39]; (7) some special enzymatic interaction could immobilize ions [40]. Fig. 1d illustrates the interactions between mushroom and ions. These functions of the living mushroom may provide a platform to engineer better transport systems, which could be maintained after carbonization. The retained transport systems from living mushroom inspire us to explore their applications for high-efficiency CDI.

In this work, we selectively cultivated mushroom (*G. lucidum*) mycelia/sporophores and carbonized them as the CDI electrode materials. The difference in natural structure and morphology dramatically influences the electrochemical desalination performances of mycelia and sporophores derived carbon (MDC and SDC). By analyzing their internal pore structure and surface chemistry, it is concluded that high surface area and heteroatomic doping surface lead to an increase in the SAC. More importantly, the efficient transport system of mycelia significantly improves the salt adsorption rate (SAR). The resultant hierarchical MDC delivers a high specific capacity of 260 F g^{-1}. The CDI devices could realize an SAC of 24.17 mg g^{-1} and rapidly remove salts from solution with a short characterization time of 2.4 min. Both the SAC and SAR of MDC exceed those of SDC and commercial active carbon (AC). This work demonstrates that the internal structure of biomass, even harvested from the different growth stages, could significantly change the performance of their derived materials in practical applications. In future, some hardly-achieved structures or transport systems may be engineered by gene-modification. Such a route differs from conventional synthesis and will certainly expand technologies for structure design or material synthesis.

2. Experimental

2.1. Mushroom cultivation

Mushroom (*Ganoderma lucidum* strain CGMCC 5.616) from the China General Microbiological Culture Collection Center was placed in a potato dextrose agar medium with 5 g L^{-1} peptone, 35 g L^{-1} sucrose, 2.5 g L^{-1} yeast extract, 1 g L^{-1} KH_2PO_4 H_2O, 0.5 g L^{-1} $MgSO_4$ $7H_2O$, and 0.05 g L^{-1} vitamin B1. To ensure that the grown strain has a high nitrogen content, we added ammonium sulfate and glutamic acid (5 g L^{-1}). Cultivation and the two-stage shake-static fermentation of *G. ludicum* were performed as described previously [41]. In the first incubation step, the fermentation solution was prepared and its pH was adjusted to 6. The mycelial suspension was added into the medium and placed on a rotary shaker (150 rpm) at 28 °C. The incubation was maintained for 7 days. In the second incubation step, the fermentation broth obtained in the first stage was mixed into the initial mycelial suspension. The ratio was 1:9. The mixture was then incubated for 5 days in a static growth period. After incubation (12 days in total), the mycelium film was washed 3 times using distilled water before the preparation of MDC.

2.2. Materials preparation of MDC

Mycelium (10 g) was washed with de-ionized water and dried at 60 °C overnight. Carbonization was conducted in a tube furnace at 500 °C for 2 h. After cooling down to room temperature, the carbonized sample was mixed with KOH by a 1:2 mass ratio and then annealed 800 °C for 3 h. The resultant MDC was cleaned with de-ionized water and 0.1 M HCl until the pH of eluate remains invariable. MDC, acetylene black, and poly (vinylidene fluoride) were mixed by a mass ratio of 8:1:1 to form a slurry in N-methylpyrrolidone. The slurry was casted on a commercial carbon paper (CeTech Corp.) with a loading of 1–2 mg cm^{-2}.

2.3. Material characterization

Morphologic observation was performed by a scanning electron microscope (SEM, Zeiss Ultra 55, USA). High-resolution transmission electron microscope (TEM) images were collected on an FEI Tecnai F20 microscope at 200 kV. X-ray photoelectron spectroscopic (XPS) spectra were recorded using an ESCALab MKII X-ray photoelectron spectrometer with Mg Kα X-ray. The binding energies in XPS analysis were corrected by referencing C 1s to 284.6 eV. The X-ray diffraction (XRD) analyses were conducted by a D/MAX2500V (Rigaku, Japan) with Cu Kα radiation (λ = 1.5418 Å). The quantification of C, H, N, and S was conducted with an element analyzer (Elementar Vario EL, Thermo Fisher). The Raman spectra were recorded using a JASCO microscope spectrometer (NRS-1000DT) with the excitation light of an air-cooled He–Ne laser at 632.8 nm wavelength.

2.4. Electrochemical measurements

All electrochemical measurements were conducted with a Biologic VSP potentiostat. The cyclic voltammetric (CV) and galvanostatic charge/discharge (GCD) were conducted in an aqueous solution of 1 M NaCl with Pt and Ag/AgCl as the counter and reference electrodes, respectively. EIS spectra was measured between 0.01 and 100 kHz. The specific capacitance (F g^{-1}) were calculated from the CV and GCD curves using the following equation:

$$C = \frac{\int id\mathrm{V}}{2{*}\Delta \mathrm{V} * \mathrm{m} * v} \tag{1}$$

$$C = \frac{I\Delta t}{\Delta V} \tag{2}$$

where i is the CV current, m is the mass, v is the scan rate, Δt is the charge/discharge time, and ΔV is the voltage window.

2.5. Desalination tests

The desalination experiments were conducted using a home-made CDI setup (10 cm × 10 cm). The samples with the same loading were used as the cathode and anode. An insulating separator (NKK-MPE30AC-10) was sandwiched between the cathode and anode. A solution of 0.5 g L^{-1} was circulated with a peristaltic pump at a flow rate of 20 mL min^{-1}. The solution conductivity was monitored with a conductivity meter (DDS-307A). The operation voltage was 1.4 V. The salt adsorption capacity (Γ, mg g^{-1}) and salt removal rate (ASAR, mg g^{-1} min^{-1}) were calculated with the following equations:

$$\Gamma = \frac{(C_t - C_0)V}{m} \tag{3}$$

$$ASAR = \frac{\Gamma}{t} \tag{4}$$

where C_0 is the initial concentration of NaCl (mg L^{-1}), C_t is the concentration at t min (mg L^{-1}), V is the volume (L), and m is the total mass of active materials (g) on the cathode and anode.

3. Results and discussion

3.1. Morphology and pore characterization

During the two-stage shake-static cultivation, the mycelium of *G. lucidum* were evenly intertwined to form a fibrous mesh-like mycelium-film from spherical aggregates [41]. Fig. 2a presents the SEM images of mushroom mycelia. The filaments of mycelia have an average diameter of 1 μm. The hollow interior could be clearly observed, forming a sharp contrast against sporophores (Fig. S1). These tubular filaments are interwoven to form a network for nutrient transport [20,42]. After carbonization and surface treatment with KOH, the filaments seem to shrink owing to the loss of volatile components while the network retains as shown in Fig. 2b (see more details in Fig. S2). The TEM image in

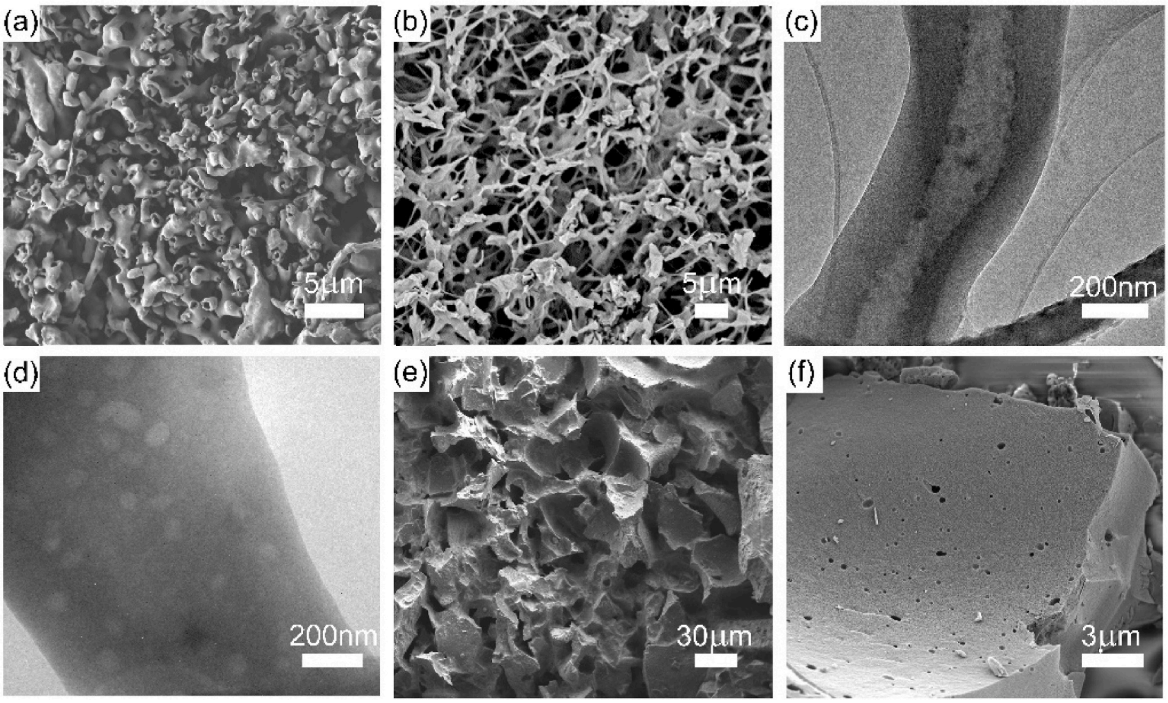

Fig. 2. Morphologic characterization: SEM images of (a) mushroom mycelium and (b) carbonized mycelium. TEM images of (c) tubular filament and (d) holey wall. (e,f) SEM images of sporophore at varied magnifications.

Fig. 2c indicates that the tubular morphology has an outer diameter of ~600 nm and internal hollow pore of 150–200 nm. A zoomed-in TEM image in Fig. 2d displays multiple 50–100 nm holes, which were generated by KOH etch during treatment [43]. These holes on the wall facilitates ions exchange in and out of tubular filaments [44]. In contrast, SDC demonstrates bulk aggregates, which have large grains size. Large channels exist between grains, also serving to transport resources when mushroom grows. By zooming into the surface of a bulk grain, a large number of small pores (100–300 nm) could be clearly observed.

To explain the pore formation, a morphology and growth analysis is necessary. It is clearly seen that despite having porous channels, the bulky sporophore and filamentous mycelium exhibit different morphologies and pore structures, which result from different growth stage and metabolism requirements [45,46]. Mycelium is the primary stage in the fungal organism's life cycle, usually with a diameter less than 30 μm [47]. The morphology of mycelia reflects an effective foraging strategy whereby mycelia form networks to transport nutrients between spatially separated source and sink regions [42,48]. The long-range transport of resources in fungal hypha had been visualized with autofluorescent molecules [49], showing the immense traffic like man-made infrastructures such as public suburban commuter railway systems [32]. Carbonization barely retains the original transport systems for nutrients in live mycelia. Such an intricate network of filaments endows MDC with internally and externally connected pore structure and provides ideal transport system for desalination. The sporophore is formed from the further differentiation of mycelium, with a larger diameter (80–100 μm) and a more irregular structure than those of mycelium [50]. In addition, the chemical composition of mushroom sporophore and mycelium are quite different [51]. The large amount of protein contained in the mycelium may also attribute to its excellent performances on mineral bioaccumulation [52]. From the viewpoint of cell growth and components, mycelia are evolved to do resource transport more efficiently than sporephores. Therefore, desalination prefers MDC over SDC owing to their different transport systems.

To further understand the pore structure, we measured N_2 adsorption/desorption isotherms. Fig. 3a shows type-I isotherms for both MDC and SDC. At the low pressure, there is an abrupt increase of adsorption, indicative of micropores, which may be formed by KOH etch and microscale organelles [43,53]. A density functional theory (DFT) method is used to analyze the pore size distribution of MDC and SDC below 10 nm. Fig. 3b shows that MDC and SDC have similar pore size distribution. Most of pores are below 4 nm and the average pore size is around 1.3 nm, indicative of a large number of micropores. The inset of Fig. 3b presents the pore distribution analysis using the Horvath-Kawazoe (H–K) method., which gives an even smaller micropore distribution with an average size of 0.56 nm. The Brunauer-Emmett-Teller (BET) method was used to determine the surface area. Notably, MDC has an extremely high surface area of 3603 m^2 g^{-1} and a pore volume of 2.2 cm^3 g^{-1} as compared to SDC (2018 m^2 g^{-1} and 1.3 cm^3 g^{-1}), indicating that mycelium is a better precursor than sporophore. Table S1 lists the pore structure parameters from BET and MIP analyses.

Surface area plays a crucial role in the surface-driven reactions. However, the BET-determined surface area is measured with N_2 adsorption, which may not truly reflect the adsorption and transport in liquid phase. Therefore, we further conducted mercury intrusion porosimetry (MIP). The MIP curves in Fig. 3c shows a steep increase in the range of 10–300 psi, which originates from large pores between bulky grains [54]. As the tap density affects the steep increase of intrusion mercury volume more significantly and could be improved by engineering with other additives when used in practical applications, we pay more attention to the pore size that is less than 5 μm (>36 psi). The volume of pores smaller than 5 μm in MDC accounts for 64.2% of total mercury intrusion volume whereas that in SDC is only 17.7% (see the pore distribution and discussion in Fig. S3). By carefully examining the cumulative volume of pores less than 200 nm, it could be seen that MDC (14.2%) has more pore volume ratio than SDC (9.3%). After extrusion, SDC contains 19% more mercury owing to narrow "bottle neck" effects. Mesopore and micropore that are characterized by the BET method provides a large surface area for ion adsorption while the good channel connection indicated by the MIP analysis can facilitate liquid-phase

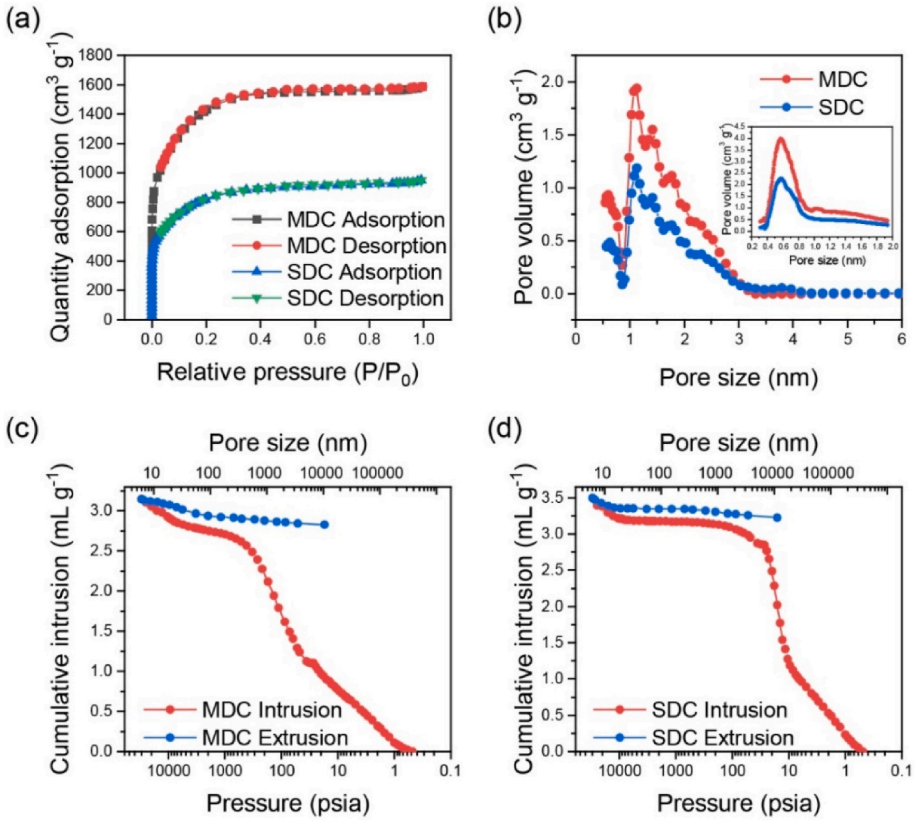

Fig. 3. Pore structural characterizations of MDC and SDC: (a) N_2 adsorption-desorption isotherms and (b) pore size distribution of MDC and SDC; MIP curves (c) MDC and (d) SDC. (A colour version of this figure can be viewed online.)

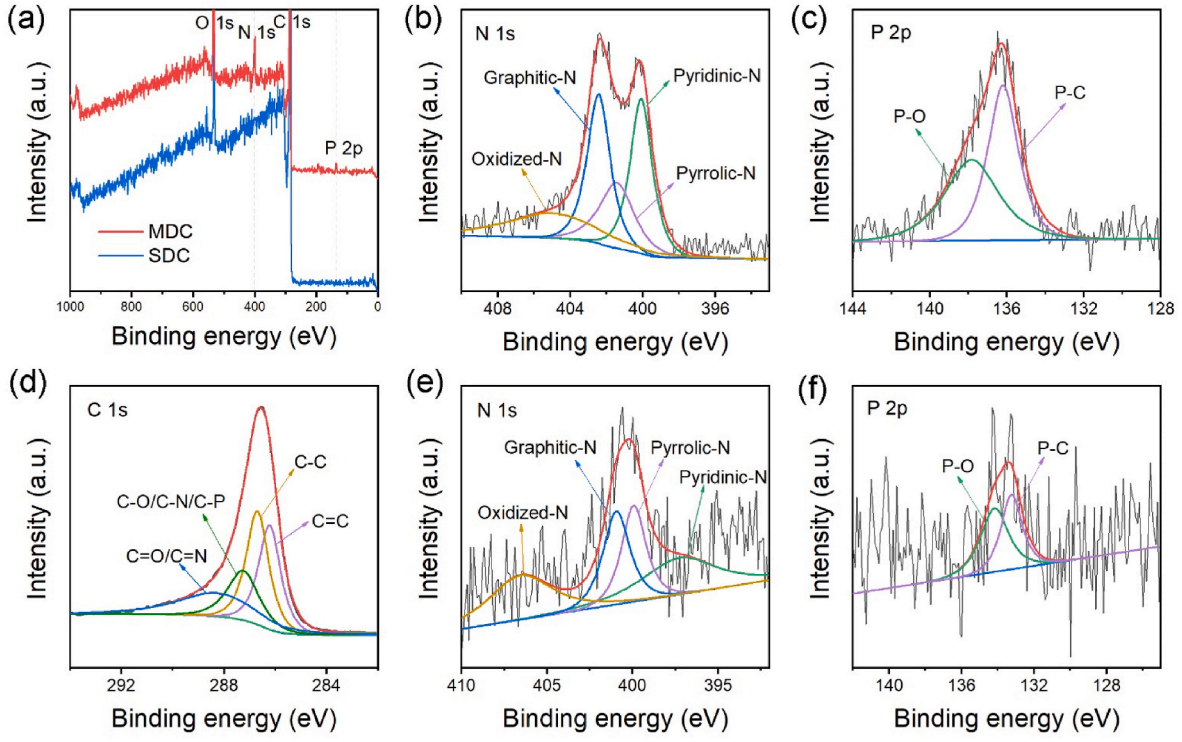

Fig. 4. Chemical composition of MDC and SDC: (a) XPS survey spectra. High-resolution XPS spectra of (b) N 1s, (c) P 2p, and (d) C 1s signals of MDC. High-resolution XPS spectra of (e) N 1s and (f) P 2p signals of SDC. (A colour version of this figure can be viewed online.)

transport of ions to the surface active sites [55,56]. As surface area and channel connection are concerned, MDC exhibits better pore structures for ion adsorption/desorption than SDC.

3.2. Surface functionality

In addition to the surface area and transport channels, surface functionality plays a second important role in adsorbing ions, which determines the desalination efficiency. Fig. 4 presents the XPS of MDC and SDC. The survey spectra in Fig. 4a indicates that both MDC and SDC contains elemental C, O, N, and P. An organic elemental quantification confirms that MDC has more N (8.22%) than SDC (1.05%) in Table S2. The XPS N 1s signals could be fitted into pyridinic-N (399.8 eV), pyrrolic-N (401.2 eV), graphitic-N (402.3 eV), and oxidized-N (404.9 eV) [57]. Graphitic- and pyrrolic- N accounts for most of N species in carbonized mushroom. The XPS P 2p signals contains two components at 137.7 eV and 136.1 eV, which correspond to P–O and P–C bonds, respectively [58,59]. In addition, the C 1s and O 1s spectra indicate that MDC contain functional groups of C–O/C–N/C–P, C═O/C═N, C–C, and C═C [60]. The XPS analyses show that N and P were doped into carbon. C═O and P–O groups could increase the hydrophilicity of MDC, which has been reported to improve the CDI performance [59]. A low contact angle in Fig. S4 indicates that MDC has better hydrophilicity than AC. Graphitic-N and C═C may enhance the conductivity of MDC [61]. The XRD patterns (Fig. S5) of MDC and SDC show no obvious peaks, indicative amorphous structure. Raman spectra (Fig. S6) display that both MDC and SDC have broad D bands and relatively weak G band intensity, indicative of rich defects. Defects may help to anchor ions. Therefore, these functionalities are believed to improve the desalination performance.

3.3. Electrochemical properties

Fig. 5a shows the cyclic voltammetric (CV) curves of MDC and SDC between 0 and 0.6 V in a solution of 1 M NaCl at a scan rate of 10 mV s^{-1}. The CV curves show nearly rectangular shapes, indicative of capacitive behavior [62]. Using equation (1), the specific capacitance of MDC is estimated to be 257.1 F g^{-1}, which is higher than that of SDC (174.6 F

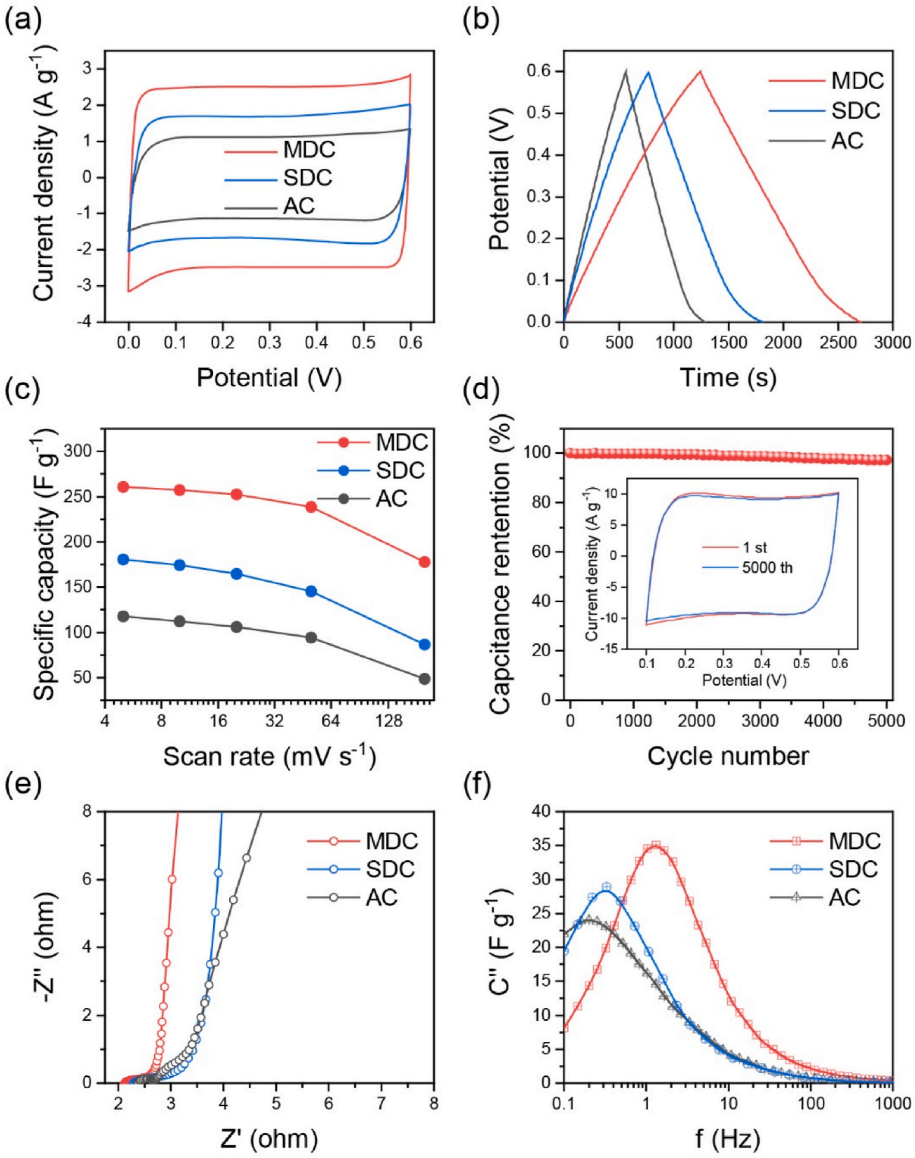

Fig. 5. Electrochemical properties of MDC, SDC and AC: (a) CV curves at a scan rate of 10 mV s^{-1}, (b) Galvanostatic charge-discharge curves at a current density of 0.1 A g^{-1}, (c) Specific capacitances at varied scan rates, (d) Capacitance retention of MDC at 50 mV s^{-1} (inset: CV curves in the 1st and 5000th cycles), (e) Nyquist plots and (f) imaginary capacitance vs frequency of MDC, SDC, and AC. (A colour version of this figure can be viewed online.)

g^{-1}). For the sake of comparison, we also measured the CV of commercial active carbon (AC) with a specific surface area of 1400 m^2 g^{-1}. Apparently, biomass-derived carbon (either MDC or SDC) demonstrates much higher specific capacitance than AC (112.2 F g^{-1}), indicating that biologically engineered materials have advantages over current commercial AC. Fig. S7 shows that at even high CV scan rates (up to 0.2 V s^{-1}), MDC could still retain nearly rectangular shape whereas SDC and AC could not, which serves as an evidence of rapid transport. Fig. 5b presents the galvanostatic charge/discharge (GCD) curves of MDC, SDC, and AC. All three samples show triangle shape curves, which are a characteristic feature of capacitors [63]. The specific capacitances of MDC, SDC, and AC are 245.7, 173.8, and 120.1 F g^{-1}, respectively. The trend is in agreement with CV measurements.

Fig. 5c displays the rate capability of MDC, SDC, and AC. At a low scan rate of 5 mV s^{-1}, MDC, SDC, and AC delivers a specific capacitance of 260.4, 180.7, and 117.5 F g^{-1}. When the scan rate increases to 200 mV s^{-1}, the specific capacitance of MDC decreases to 178.1 F g^{-1} while those of SDC and AC decrease to 86.2 F g^{-1} and 48.6 F g^{-1}, respectively. The rapid decay at high rates shows low rate capabilities, which is related to the poor transport system as indicated by the SEM and MIP analyses. At low rates, ions could be transported to active sites with low resistance. However, poorly connected channels of SDC dramatically increase the apparent resistance of ions at high rates, thereby leading to low capacitances. The transport-limited poor rate capability is also manifested by the low mercury extrusion in MIP analyses. Conversely, MDC demonstrates high rate capability owing to the interconnected channels [55,64]. The long-term cycling in Fig. 5d shows that MDC could retain 97.2% of its initial capacitance in 5000 cycles and the CV curves of the 1st and 5000th cycles are well overlapped, indicative of good cycling stability.

Fig. 5e presents the electrochemical impedance spectroscopic (EIS) measurements. The Nyquist plots of all three samples consist of much depressed semicircles and almost vertical tails. The long tails at low frequency ranges indicates the capacitive behavior [65]. The high-frequency intercept at the real axis corresponds to the intrinsic Ohmic resistance. The diameter of semicircles represents the charge transfer resistance [66]. A low intercept and short diameter of the semicircle indicate that MDC has low internal resistance and charge transfer resistance. AC exhibits generally higher impedances at each frequency than MDC and SDC, indicative of low transport properties. In consideration of typical capacitive behavior, we studied the specific capacitance with respect to frequency and plot the imagery part of capacitance in Fig. 5f. The maximum of each curves defines a time constant, τ_0, at which half of the low-frequency capacitance is reached. MDC shows a lower τ_0 of 0.76 s than SDC (3.07 s) and AC (4.95 s), indicative of a short relaxation time or rapid transport dynamics [65, 67]. To further confirm the rapid transport, we analyzed the relationship between the CV peak current (i_p) and scan rates (υ). Fig. S8a show the slope of log (i_p) vs υ is close to 1.0, indicative of surface capacitive behavior. The EIS measurements allow us to obtain the diffusion coefficient of ions in MDC is much higher than those in SDC and AC (see details in Fig. S8 and the discussion).

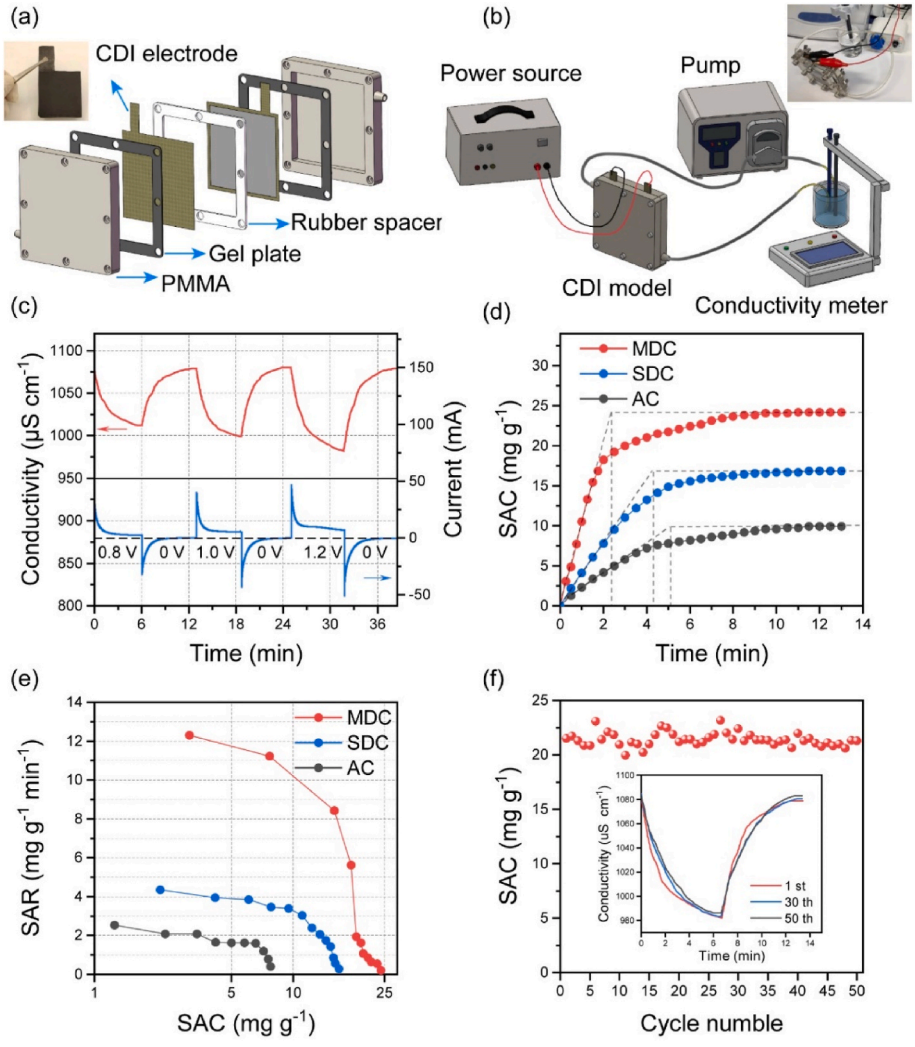

Fig. 6. CDI properties that were measured in a 500 mg L^{-1} NaCl solution: (a) Illustration of each component of a CDI model; (b) Optical image and illustration of the desalination system, (c) Desalination cycling curves at varied voltages of MDC, (d) Desalination profiles of MDC, SDC and AC at 1.4 V in a 0.5 g L^{-1} NaCl solution, (e) Ragone plots of SAR vs SAC of MDC, SDC, and AC, (f) Cycling stability of MDC at 1.2 V. (the inset is the conductivity curves in the 1st and 50th cycles). (A colour version of this figure can be viewed online.)

3.4. CDI performance

To evaluate the CDI performance, we assembled symmetric cell using MDC, SDC, and AC as the electrodes, respectively. Fig. 6a presents the CDI module and its assembly. Salt concentrations were measured with a conductivity meter as shown in Fig. 6b. A dynamic test was first applied with varied voltage (0.8, 1.0, and 1.2V) on the MDC cell sequentially to demonstrate the desalination process. Each voltage was held for 6 min and then switched to recover the conductivity to the initial value. Fig. 6c shows that upon polarization, the solution conductivity decreased exponentially with the time, indicative of the adsorption of Na^+ and Cl^-. When the voltage polarity was switched, the conductivity increased again owing to the desorption [13,68].

Fig. 6d displays the salt removal capacity with the time. All three cells exhibit an approximately linear increase in salt removal and eventually reach saturated adsorption levels. The SAC increases with the salt concentration and voltage as shown in Fig. S9. MDC demonstrates a much higher salt removal capacity of 24.2 mg g^{-1} in a solution of 500 mg L^{-1} NaCl. By contrast, SDC and AC could remove only 16.8 and 9.5 mg g^{-1} salt. By extrapolating the linear part to the saturated adsorption levels, we could obtain a characteristic time, which is a convenient parameter to reflect how fast the cell reaches saturation. MDC has the shortest characteristic time of ~2.4 min, which is faster than SDC (4.3 min) and AC (5.1 min), indicating that MDC could remove salt rapidly. From the viewpoint of either SAC or SAR as shown in Fig. 6e, MDC dramatically exceeds SDC and AC, showing the highest desalination capability and rates. As compared to previous reports (Table S3), the efficient transport network of mycelia endows MDC with the highest salt removal rate of 12.31 mg g^{-1} min^{-1}. Furthermore, MDC enables the highest charge efficiency of 82% and the lowest energy consumption of 0.624 Wh g^{-1} as shown in Fig. S10. At last, the cycling properties were tested in a solution of 0.5 mg L^{-1} at 1.2 V (Fig. 6f). Although there exists a minor variation of SAC (which may result from the errors of concentration analysis), the average SAC remains almost constant for 50 cycles, demonstrating good cycling stability.

4. Conclusion

In summary, we propose to cultivate and carbonize mushroom mycelia for the applications of capacitive deionization. Mycelia and sporophores are two typical growth stages or different parts of mushroom. Mycelia are usually neglected because of its existence underground. Mushroom evolves to develop their intricate network of tubular filaments for efficient nutrients transport. Such an excellent transport system endowed by nature works the similar way for the CDI, offering the opportunity to enhance the electrochemical desalination performance. Our technology maximizes filamentous network during mushroom culture, retains the naturally-evolved transport network, and increases surface area and pore connection. As a result, MDC delivers a high capacity of 260.4 F g^{-1} and demonstrates the highest salt removal capacity of 24.2 mg g^{-1}. Even at high rates, MDC also exceeds SDC and commercial active carbon with a much short characteristic time of 2.4 min, showing the rapid salty removal rate (12.31 mg g^{-1} min^{-1}). This work demonstrates that high-efficiency transport system of mycelium could be used to enhance electrochemical desalination and prospectively provides a platform of gene-editing transport system for better desalination in future.

CRediT authorship contribution statement

Chen Zhao: Experiment, Writing – original draft. **Qin Wang:** Experiment, Writing – original draft. **Shaozhong Chang:** Data curation, Formal analysis. **Shuo Zhang:** Data curation, Formal analysis. **Zhonghua Li:** ValidationValudation. **Zihan Shen:** Material synthesis. **Xin Jin:** Characterization. **Han Xiao:** Conceptualization, Supervision. **Huigang Zhang:** Conceptualization, Supervision, All authors discussed results and wrote the manuscript.

Declaration of competing interest

The authors declare that they have no known competing financial interests or personal relationships that could have appeared to influence the work reported in this paper.

Acknowledgments

The authors acknowledge the financial support of the National Key R&D Program of China (No. 2020YFA0406104), the National Natural Science Foundation of China (Nos. 22075131), and the State Key Laboratory of Multiphase Complex Systems (No. MPCS-2021-A).

Appendix A. Supplementary data

Supplementary data to this article can be found online at https://doi.org/10.1016/j.carbon.2022.05.020.

References

[1] M.A. Shannon, P.W. Bohn, M. Elimelech, J.G. Georgiadis, B.J. Mariñas, A. M. Mayes, Science and technology for water purification in the coming decades, Nature 452 (2008) 301–310, https://doi.org/10.1038/nature06599.
[2] A.M. Alklaibi, N. Lior, Membrane-distillation desalination: status and potential, Desalination 171 (2005) 111–131, https://doi.org/10.1016/j.desal.2004.03.024.
[3] C. Fritzmann, J. Löwenberg, T. Wintgens, T. Melin, State-of-the-art of reverse osmosis desalination, Desalination 216 (2007) 1–76, https://doi.org/10.1016/j.desal.2006.12.009.
[4] H. Strathmann, Electrodialysis, a mature technology with a multitude of new applications, Desalination 264 (2010) 268–288, https://doi.org/10.1016/j.desal.2010.04.069.
[5] Y. Oren, Capacitive deionization (CDI) for desalination and water treatment - past, present and future (a review), Desalination 228 (2008) 10–29, https://doi.org/10.1016/j.desal.2007.08.005.
[6] M.E. Suss, V. Presser, Water desalination with energy storage electrode materials, Joule 2 (2018) 10–15, https://doi.org/10.1016/j.joule.2017.12.010.
[7] P. Srimuk, X. Su, J. Yoon, D. Aurbach, V. Presser, Charge-transfer materials for electrochemical water desalination, ion separation and the recovery of elements, Nat. Rev. Mater. 5 (2020) 517–538, https://doi.org/10.1038/s41578-020-0193-1.
[8] S. Porada, R. Zhao, A. van der Wal, V. Presser, P.M. Biesheuvel, Review on the science and technology of water desalination by capacitive deionization, Prog. Mater. Sci. 58 (2013) 1388–1442, https://doi.org/10.1016/j.pmatsci.2013.03.005.
[9] D.V. Cuong, B.M. Matsagar, M. Lee, MdS.A. Hossain, Y. Yamauchi, M. Vithanage, et al., A critical review on biochar-based engineered hierarchical porous carbon for capacitive charge storage, Renew. Sustain. Energy Rev. 145 (2021), 111029, https://doi.org/10.1016/j.rser.2021.111029.
[10] M.E. Suss, S. Porada, X. Sun, P.M. Biesheuvel, J. Yoon, V. Presser, Water desalination via capacitive deionization: what is it and what can we expect from it? Energy Environ. Sci. 8 (2015) 2296–2319, https://doi.org/10.1039/C5EE00519A.
[11] S. Nadakatti, M. Tendulkar, M. Kadam, Use of mesoporous conductive carbon black to enhance performance of activated carbon electrodes in capacitive deionization technology, Desalination 268 (2011) 182–188, https://doi.org/10.1016/j.desal.2010.10.020.
[12] D. Xu, Y. Tong, T. Yan, L. Shi, D. Zhang, N,P-codoped meso-/microporous carbon derived from biomass materials via a dual-activation strategy as high-performance electrodes for deionization capacitors, ACS Sustain. Chem. Eng. 5 (2017) 5810–5819, https://doi.org/10.1021/acssuschemeng.7b00551.
[13] P. Zhang, P.A. Fritz, K. Schroën, H. Duan, R.M. Boom, M.B. Chan-Park, Zwitterionic polymer modified porous carbon for high-performance and antifouling capacitive desalination, ACS Appl. Mater. Interfaces 10 (2018) 33564–33573, https://doi.org/10.1021/acsami.8b11708.
[14] J. Kim, J.H. Kim, H.S. Park, Hierarchically open-porous nitrogen-incorporated carbon polyhedrons derived from metal-organic frameworks for improved CDI performance, Chem. Eng. J. 382 (2020), 122996, https://doi.org/10.1016/j.cej.2019.122996.
[15] J. Kim, M.S. Choi, K.H. Shin, M. Kota, Y. Kang, S. Lee, et al., Rational design of carbon nanomaterials for electrochemical sodium storage and capture, Adv. Mater. 31 (2019), 1803444, https://doi.org/10.1002/adma.201803444.
[16] Y. Wang, S.E. Naleway, B. Wang, Biological and bioinspired materials: structure leading to functional and mechanical performance, Bioact. Mater. 5 (2020) 745–757, https://doi.org/10.1016/j.bioactmat.2020.06.003.
[17] Z. Wang, W. Zhu, Y. Qiu, X. Yi, A. von dem Bussche, A. Kane, et al., Biological and environmental interactions of emerging two-dimensional nanomaterials, Chem. Soc. Rev. 45 (2016) 1750–1780, https://doi.org/10.1039/C5CS00914F.
[18] M.A. Meyers, P.-Y. Chen, A.Y.-M. Lin, Y. Seki, Biological materials: structure and mechanical properties, Prog. Mater. Sci. 53 (2008) 1–206, https://doi.org/10.1016/j.pmatsci.2007.05.002.

[19] H. Ronellenfitsch, Optimal elasticity of biological networks, Phys. Rev. Lett. 126 (2021), 038101, https://doi.org/10.1103/PhysRevLett.126.038101.
[20] M.R. Islam, G. Tudryn, R. Bucinell, L. Schadler, R.C. Picu, Morphology and mechanics of fungal mycelium, Sci. Rep. 7 (2017) 13070, https://doi.org/10.1038/s41598-017-13295-2.
[21] X. Liu, Y. Wu, X. Xu, Y. Li, Y. Zhang, B. Li, Bio-Conveyor Belts: bidirectional transport of nanoparticles and cells with a bio-conveyor belt, Small 15 (2019), 1970274, https://doi.org/10.1002/smll.201970274.
[22] N. Ghanem, C.E. Stanley, H. Harms, A. Chatzinotas, L.Y. Wick, Mycelial effects on phage retention during transport in a microfluidic platform, Environ. Sci. Technol. 53 (2019) 11755–11763, https://doi.org/10.1021/acs.est.9b03502.
[23] W. Wu, J. Pu, J. Wang, Z. Shen, H. Tang, Z. Deng, et al., Biomimetic bipolar microcapsules derived from *staphylococcus aureus* for enhanced properties of lithium-sulfur battery cathodes, Adv. Energy Mater. 8 (2018), 1702373, https://doi.org/10.1002/aenm.201702373.
[24] H. Dou, M. Xu, B. Jiang, G. Wen, L. Zhao, B. Wang, et al., Bioinspired graphene oxide membranes with dual transport mechanisms for precise molecular separation, Adv. Funct. Mater. 29 (2019), 1905229, https://doi.org/10.1002/adfm.201905229.
[25] W. Chen, T. Dong, Y. Xiang, Y. Qian, X. Zhao, W. Xin, et al., Ionic crosslinking-induced nanochannels: nanophase separation for ion transport promotion, Adv. Mater. 34 (2022), 2108410, https://doi.org/10.1002/adma.202108410.
[26] J. Kim, Y. Yi, D.-H. Peck, S.-H. Yoon, D.-H. Jung, H.S. Park, Controlling hierarchical porous structures of rice-husk-derived carbons for improved capacitive deionization performance, Environ. Sci.: Nano 6 (2019) 916–924, https://doi.org/10.1039/C8EN01181H.
[27] S. Zhao, T. Yan, Z. Wang, J. Zhang, L. Shi, D. Zhang, Removal of NaCl from saltwater solutions using micro/mesoporous carbon sheets derived from watermelon peel via deionization capacitors, RSC Adv. 7 (2017) 4297–4305, https://doi.org/10.1039/C6RA27127H.
[28] R. Zhang, X. Gu, Y. Liu, D. Hua, M. Shao, Z. Gu, et al., Hydrophilic nano-porous carbon derived from egg whites for highly efficient capacitive deionization, Appl. Surf. Sci. 512 (2020), 145740, https://doi.org/10.1016/j.apsusc.2020.145740.
[29] J.S. Kang, S. Kim, D.Y. Chung, Y.J. Son, K. Jo, X. Su, et al., Rapid inversion of surface charges in heteroatom-doped porous carbon: a route to robust electrochemical desalination, Adv. Funct. Mater. 30 (2020), 1909387, https://doi.org/10.1002/adfm.201909387.
[30] Z. Xie, X. Shang, J. Yan, T. Hussain, P. Nie, J. Liu, Biomass-derived porous carbon anode for high-performance capacitive deionization, Electrochim. Acta 290 (2018) 666–675, https://doi.org/10.1016/j.electacta.2018.09.104.
[31] Y. Sag, T. Kutsal, Recent trends in the biosorption of heavy metals: a review, Biotechnol. Bioproc. Eng. 6 (2001) 376–385, https://doi.org/10.1007/BF02932318.
[32] H. Harms, D. Schlosser, L.Y. Wick, Untapped potential: exploiting fungi in bioremediation of hazardous chemicals, Nat. Rev. Microbiol. 9 (2011) 177–192, https://doi.org/10.1038/nrmicro2519.
[33] X. Wang, X. Li, G. Liu, Y. He, C. Chen, X. Liu, et al., Mixed heavy metal removal from wastewater by using discarded mushroom-stick biochar: adsorption properties and mechanisms, Environ. Sci.: Process. Impacts 21 (2019) 584–592, https://doi.org/10.1039/C8EM00457A.
[34] S. Siddiquee, K. Rovina, S.A. Azad, Heavy metal contaminants removal from wastewater using the potential filamentous fungi biomass: a review, J. Microb. Biochem. Technol. 7 (2015), https://doi.org/10.4172/1948-5948.1000243.
[35] R. Agerer, Fungal relationships and structural identity of their ectomycorrhizae, Mycol. Prog. 5 (2006) 67–107, https://doi.org/10.1007/s11557-006-0505-x.
[36] E. López Errasquín, C. Vázquez, Tolerance and uptake of heavy metals by trichoderma atroviride isolated from sludge, Chemosphere 50 (2003) 137–143, https://doi.org/10.1016/S0045-6535(02)00485-X.
[37] R.K. Mehra, D.R. Winge, Metal ion resistance in fungi: molecular mechanisms and their regulated expression, J. Cell. Biochem. 45 (1991) 30–40, https://doi.org/10.1002/jcb.240450109.
[38] A. Delgado, A.M. Anselmo, J.M. Novais, Heavy metal biosorption by dried powdered mycelium of *Fusarium flocciferum*, Water Environ. Res. 70 (1998) 370–375, https://doi.org/10.2175/106143098X125019.
[39] L. Dusengemungu, G. Kasali, C. Gwanama, K.O. Ouma, Recent advances in biosorption of copper and cobalt by filamentous fungi, Front. Microbiol. 11 (2020), 582016, https://doi.org/10.3389/fmicb.2020.582016.
[40] H. Tsai, R. Doong, Simultaneous determination of pH, urea, acetylcholine and heavy metals using array-based enzymatic optical biosensor, Biosens. Bioelectron. 20 (2005) 1796–1804, https://doi.org/10.1016/j.bios.2004.07.008.
[41] Q.-H. Fang, J.-J. Zhong, Two-stage culture process for improved production of ganoderic acid by liquid fermentation of higher fungus ganoderma lucidum, Biotechnol. Prog. 18 (2002) 51–54, https://doi.org/10.1021/bp010136g.
[42] M.D. Fricker, J.A. Lee, D.P. Bebber, M. Tlalka, J. Hynes, P.R. Darrah, et al., Imaging complex nutrient dynamics in mycelial networks, J. Microsc. 231 (2008) 317–331, https://doi.org/10.1111/j.1365-2818.2008.02043.x.
[43] P. Han, Selective etching of C-N bonds for preparation of porous carbon with ultrahigh specific surface area and superior capacitive performance, Energy Storage Mater. (2020) 9.
[44] M. Rose, Y. Korenblit, E. Kockrick, L. Borchardt, M. Oschatz, S. Kaskel, et al., Hierarchical micro- and mesoporous carbide-derived carbon as a high-performance electrode material in supercapacitors, Small 7 (2011) 1108–1117, https://doi.org/10.1002/smll.201001898.
[45] N.P. Money, Action and inertia in the study of hyphal growth, Fungal Biol. Rev. (2021), S1749461321000415, https://doi.org/10.1016/j.fbr.2021.09.001.
[46] M. Sánchez-García, M. Ryberg, F.K. Khan, T. Varga, L.G. Nagy, D.S. Hibbett, Fruiting body form, not nutritional mode, is the major driver of diversification in mushroom-forming fungi, Proc. Natl. Acad. Sci. U.S.A. 117 (2020) 32528–32534, https://doi.org/10.1073/pnas.1922539117.
[47] M.R. Islam, G. Tudryn, R. Bucinell, L. Schadler, R.C. Picu, Morphology and mechanics of fungal mycelium, Sci. Rep. 7 (2017) 13070, https://doi.org/10.1038/s41598-017-13295-2.
[48] S.S. Schmieder, C.E. Stanley, A. Rzepiela, D. van Swaay, J. Sabotič, S.F. Nørrelykke, et al., Bidirectional propagation of signals and nutrients in fungal networks via specialized hyphae, Curr. Biol. 29 (2019) 217–228, https://doi.org/10.1016/j.cub.2018.11.058, e4.
[49] R. Dong, W. Li, Y. Kang, X. Yang, S. Qu, X. Zhang, et al., Uptake, translocation and toxicity of fluorescent carbon dots in oyster mushroom (Pleurotus ostreatus), J. Lumin. 235 (2021), 118010, https://doi.org/10.1016/j.jlumin.2021.118010.
[50] G. Balzamo, N. Singh, N. Wang, G.T. Vladisavljević, G. Bolognesi, E. Mele, 3D arrays of super-hydrophobic microtubes from polypore mushrooms as naturally-derived systems for oil absorption, Materials 12 (2019) 132, https://doi.org/10.3390/ma12010132.
[51] B.F. Lau, N. Abdullah, N. Aminudin, Chemical composition of the tiger's milk mushroom, *lignosus rhinocerotis* (cooke) ryvarden, from different developmental stages, J. Agric. Food Chem. 61 (2013) 4890–4897, https://doi.org/10.1021/jf4002507.
[52] E. Ulziijargal, J.-L. Mau, Nutrient compositions of culinary-medicinal mushroom fruiting bodies and mycelia, Int. J. Med. Mushrooms 13 (2011) 343–349, https://doi.org/10.1615/IntJMedMushr.v13.i4.40.
[53] P. Wang, H. Ye, Y.-X. Yin, H. Chen, Y.-B. Bian, Z.-R. Wang, et al., Fungi-enabled synthesis of ultrahigh-surface-area porous carbon, Adv. Mater. 31 (2019), 1805134, https://doi.org/10.1002/adma.201805134.
[54] J. Li, N. Zhang, H. Zhao, Z. Li, B. Tian, Y. Du, Cornstalk-derived macroporous carbon materials with enhanced microwave absorption, J. Mater. Sci. Mater. Electron. 32 (2021) 25758–25768, https://doi.org/10.1007/s10854-020-04571-5.
[55] C. Kim, P. Srimuk, J. Lee, S. Fleischmann, M. Aslan, V. Presser, Influence of pore structure and cell voltage of activated carbon cloth as a versatile electrode material for capacitive deionization, Carbon 122 (2017) 329–335, https://doi.org/10.1016/j.carbon.2017.06.077.
[56] Y. Gao, R. Liu, H. Jing, W. Chen, Q. Yin, Hydraulic properties of single fractures grouted by different types of carbon nanomaterial-based cement composites, Bull. Eng. Geol. Environ. 79 (2020) 2411–2421, https://doi.org/10.1007/s10064-019-01707-8.
[57] H. Wang, H. Deng, Y. He, L. Huang, D. Wei, T. Hao, et al., Facile and sustainable synthesis of slit-like microporous N-doped carbon with unexpected electrosorption performance, Chem. Eng. J. 396 (2020), 125249, https://doi.org/10.1016/j.cej.2020.125249.
[58] J. Han, L. Shi, T. Yan, J. Zhang, D. Zhang, Removal of ions from saline water using N, P co-doped 3D hierarchical carbon architectures *via* capacitive deionization, Environ. Sci.: Nano 5 (2018) 2337–2345, https://doi.org/10.1039/C8EN00652K.
[59] H. Zhang, C. Wang, W. Zhang, M. Zhang, J. Qi, J. Qian, et al., Nitrogen, phosphorus co-doped eave-like hierarchical porous carbon for efficient capacitive deionization, J. Mater. Chem. A. 9 (2021) 12807–12817, https://doi.org/10.1039/D0TA10797B.
[60] S. Hu, K. Xie, X. Zhang, S. Zhang, J. Gao, H. Song, et al., Significantly enhanced capacitance deionization performance by coupling activated carbon with triethyltetramine-functionalized graphene, Chem. Eng. J. 384 (2020), 123317, https://doi.org/10.1016/j.cej.2019.123317.
[61] Y. Li, Y. Liu, J. Shen, J. Qi, J. Li, X. Sun, et al., Design of nitrogen-doped cluster-like porous carbons with hierarchical hollow nanoarchitecture and their enhanced performance in capacitive deionization, Desalination 430 (2018) 45–55, https://doi.org/10.1016/j.desal.2017.12.040.
[62] P. Simon, Y. Gogotsi, Perspectives for electrochemical capacitors and related devices, Nat. Mater. 19 (2020) 1151–1163, https://doi.org/10.1038/s41563-020-0747-z.
[63] P. Zhang, J. Li, M.B. Chan-Park, Hierarchical porous carbon for high-performance capacitive desalination of brackish water, ACS Sustain. Chem. Eng. 8 (2020) 9291–9300, https://doi.org/10.1021/acssuschemeng.0c00515.
[64] D. Schneider, D. Mehlhorn, P. Zeigermann, J. Kärger, R. Valiullin, Transport properties of hierarchical micro–mesoporous materials, Chem. Soc. Rev. 45 (2016) 3439–3467, https://doi.org/10.1039/C5CS00715A.
[65] F. Wei, X. He, L. Ma, H. Zhang, N. Xiao, J. Qiu, 3D N,O-codoped egg-box-like carbons with tuned channels for high areal capacitance supercapacitors, Nano-Micro Lett. 12 (2020) 82, https://doi.org/10.1007/s40820-020-00416-2.
[66] S. Zhao, T. Yan, H. Wang, J. Zhang, L. Shi, D. Zhang, Creating 3D hierarchical carbon architectures with micro-, meso-, and macropores via a simple self-blowing strategy for a flow-through deionization capacitor, ACS Appl. Mater. Interfaces 8 (2016) 18027–18035, https://doi.org/10.1021/acsami.6b03704.
[67] G. Li, K. Mao, M. Liu, M. Yan, J. Zhao, Y. Zeng, et al., Achieving ultrahigh volumetric energy storage by compressing nitrogen and sulfur dual-doped carbon nanocages via capillarity, Adv. Mater. 32 (2020), 2004632, https://doi.org/10.1002/adma.202004632.
[68] G. Tan, S. Lu, N. Xu, D. Gao, X. Zhu, Pseudocapacitive behaviors of polypyrrole grafted activated carbon and MnO_2 electrodes to enable fast and efficient membrane-free capacitive deionization, Environ. Sci. Technol. 54 (2020) 5843–5852, https://doi.org/10.1021/acs.est.9b07182.